MATERIALS SCIENCE

Integrated design of aluminum-enriched high-entropy refractory B2 alloys with synergy of high strength and ductility

Jie Qi[1]*, Xuesong Fan[2], Diego Ibarra Hoyos[1], Michael Widom[3,4], Peter K. Liaw[2]*, Joseph Poon[1,5]*

Refractory high-entropy alloys (RHEAs) are promising high-temperature structural materials. Their large compositional space poses great design challenges for phase control and high strength-ductility synergy. The present research pioneers using integrated high-throughput machine learning with Monte Carlo simulations supplemented by ab initio calculations to effectively navigate phase selection and mechanical property predictions, developing single-phase ordered B2 aluminum-enriched RHEAs (Al-RHEAs) demonstrating high strength and ductility. These Al-RHEAs achieve remarkable mechanical properties, including compressive yield strengths up to 1.7 gigapascals, fracture strains exceeding 50%, and notable high-temperature strength retention. They also demonstrate a tensile yield strength of 1.0 gigapascals with a ductility of 9%, albeit with B2 ordering. Furthermore, we identify valence electron count domains for alloy ductility and brittleness with the explanation from density functional theory and provide crucial insights into elemental influence on atomic ordering and mechanical performance. The work sets forth a strategic blueprint for high-throughput alloy design and reveals fundamental principles governing the mechanical properties of advanced structural alloys.

INTRODUCTION

In the ceaseless quest to defy extreme temperatures and hostile environments, high-performance alloys become indispensable in aerospace, automotive, and power generation sectors. Conventional Ni/Co-based superalloys, despite their thermal stability and high-temperature mechanical properties, have inevitably encountered inherent performance ceilings, such as a melting point below 1500°C. The past decade has seen the advent of high-entropy alloys (HEAs) (*1*) with revolutionized performance. The refractory high-entropy alloys (RHEAs), comprising refractory elements, Ti, V, Cr, Zr, Nb, Mo, Hf, Ta, and W, have stood out for elevated-temperature applications with high strength and ductility (*2*, *3*). However, their broader adoption faces challenges, such as high cost, densities, and poor oxidation resistance. Al-containing RHEAs (Al-RHEAs) resembling aluminides have emerged as a solution (*4*–*7*), with the Al incorporation yielding cost/density reductions, and enhanced oxidation and corrosion resistance (*8*, *9*). Moreover, Al inclusion typically induces the formation of an ordered body-centered-cubic (BCC)–derivative (B2) phase within the disordered BCC matrix (*10*–*12*), further strengthening the alloys. This B2-BCC morphology sometimes undergoes the "phase inversion" (*5*), a transformation of a continuous, channel-like B2 phase into discontinuous B2 phases surrounded by a BCC matrix after extended annealing, highlighting the thermal instability of the mixed BCC-B2 phase configuration compared to the stable γ′-γ phases for Ni/Co-based superalloys.

Despite the noteworthy advantages of Al-RHEAs, their design inevitably introduces specific challenges. Most Al-RHEAs demonstrate limited ductility. The strong p-d electron interaction between the Al and refractory elements can precipitate brittle intermetallic phases (IMs) (*11*, *13*). The dislocation movement impediment from B2 long-range ordering (LRO) and the reduced slip planes from the BCC to B2 phase further limit their ductility (*10*). Excluding the mostly brittle Al-RHEAs due to the formation of Laves phases or other brittle IMs (*11*, *14*), those composed solely of a B2 phase or BCC + B2 composite phase also seldom exhibit plasticity or ductility. For example, Al-RHEAs from the AlNbTiV (*11*, *13*), AlCrNbTiV (*13*), AlNbTaTiZr (*14*, *15*), AlNbTaTiVZr (*15*), AlCrMoTi (*10*), and AlMoNbTiV (*16*) systems have been documented to display compressive plasticity limited to a maximum of 6% at room temperature. Therefore, careful phase and B2-LRO control becomes imperative. Besides, the design challenge resides in effectively navigating the vast HEA compositional space and optimizing manifold materials' properties simultaneously to achieve the Pareto front. The conventional trial-and-error approaches have become obsolete, making integrated computational material engineering (ICME) vital in material exploration (*17*–*20*). Moreover, how various material parameters fundamentally influence alloy formation and ductility is yet to be fully elucidated, which remains an area of substantial research focus.

The present work features three core innovations that address the aforementioned challenges: First, a comprehensive alloy-design strategy merges the cutting-edge machine learning (ML) models with an enhanced ICME framework combined with Monte Carlo (MC) simulations, ab initio molecular dynamics (AIMD) simulations, ab initio relaxation, and classical computational methodologies, enabling high-throughput HEA predictions, effectively pinpointing potential high-performance alloys, and reducing experimental efforts. Second, joint endeavors from experiments and MC studies successfully optimize a series of single B2-phase AlHfNbTi(V) HEAs, exhibiting superior strength and ductility, compared to typical plasticity-constrained B2 Al-RHEAs, highlighting aluminum's role in atomic ordering and plasticity control. Third, a prominent correlation between the valence electron count (VEC) (*21*) and alloy ductility elucidated in light of density functional theory (DFT) calculations underscores VEC's importance within the property-prediction paradigm.

[1]Department of Physics, University of Virginia, Charlottesville, VA 22904, USA. [2]Department of Materials Science and Engineering, The University of Tennessee, Knoxville, TN 37996, USA. [3]Department of Physics, Carnegie Mellon University, Pittsburgh, PA 15213, USA. [4]Department of Materials Science and Engineering, Carnegie Mellon University, Pittsburgh, PA 15213, USA. [5]Department of Materials Science and Engineering, University of Virginia, Charlottesville, VA 22904, USA.
*Corresponding author. Email: sjp9x@virginia.edu (J.P.); pliaw@utk.edu (P.K.L.); jq4xa@virginia.edu (J.Q.)

Moving forward, this article will provide insights into a high-performance HEAs development methodology via ICME and theory-guided efficient compositional tuning. It delves into fundamental phenomena regarding the elemental influence on atomic ordering and the role of electronic structures on HEA-mechanical properties, laying a foundation for future alloy development and inspiring research in this field.

RESULTS

ICME model construction and results

The ICME model (Fig. 1) integrates phases and property prediction modules to design Al-RHEAs with high strengths and ductility. Considering phase predictions, CALPHAD (CALculation of PHAse Diagrams) frequently identifies Al-RHEAs' Al-X-Y type (X and Y are refractory elements) B2-strengthening phase (*22*) as the BCC matrix (*22*, *23*). Therefore, we adopt ML models trained specifically for Al-X-Y B2 and other phases [detailed in our prior work (*24*, *25*)], which integrate innovatively designed phase-diagram features (*24*) with traditional Hume-Rothery and thermodynamic features (*26*), and are enhanced by feature engineering for improved accuracy. Trained on a database of ~ 1000 HEAs and comprehensively validated by experiments, the ML models can predict nine phases with around 90% accuracy. Our targeted phases allow a solid-solution matrix and strengthening B2 phase in an as-cast condition, potentially exhibiting ductility, as predicted by subsequent ML mechanical property prediction models. Notably, while face-centered-cubic (FCC) and hexagonal close-packed (HCP) phases are permissible, they have not been predicted by ML to form in our Al-enriched RHEAs. Meanwhile, we aim to circumvent noncubic Laves and Sigma phases, which can embrittle the alloy due to the precipitate-matrix strain incompatibility, acting as stress concentrators and promoting crack initiation and propagation and leading to alloy early failure (*11*, *13*, *14*). In addition, despite the Heusler phase's potential as a coherent strengthening phase in alloys with FCC matrices (*18*), its relevance is limited in Al-RHEAs due to the absence of an FCC matrix and will be avoided.

Predictions of mechanical properties, such as compressive yield strength, σ_{YS}, and fracture strain, ε_f, are conducted with ML models. Additional properties, including melting temperature, T_{melt} (Eq. 9), density, ρ (Eq. 10), and Poisson's ratio, $\bar{\nu}$ (table S1), are determined through separate calculations. The ML mechanical property prediction models select the optimal feature combinations by a genetic algorithm (GA) (*27*) (details in Methods) from a total of 16 initial physics-based features (table S1), with some computed by the effective medium calculation (EMC) method (*28*) to reduce the computational burden while maintaining fidelity to experimental or DFT-calculated values. The EMC's effectiveness is exemplified in the D-parameter calculation (*29*) (detailed in Methods), whose DFT-calculated values show a direct correlation with the BCC HEAs' ε_f (*29*, *30*). The EMC-computed D parameter is well aligned with the DFT-calculated values (*29*) with a mere 5% absolute mean error (Fig. 2A), demonstrating a fast and reliable alternate calculation for high-throughput and ICME applications.

Most current ML-based mechanical property models are tailored to specific HEA phases to enhance prediction accuracies by focusing on phase-specific properties controlling mechanisms. The ICME-designed

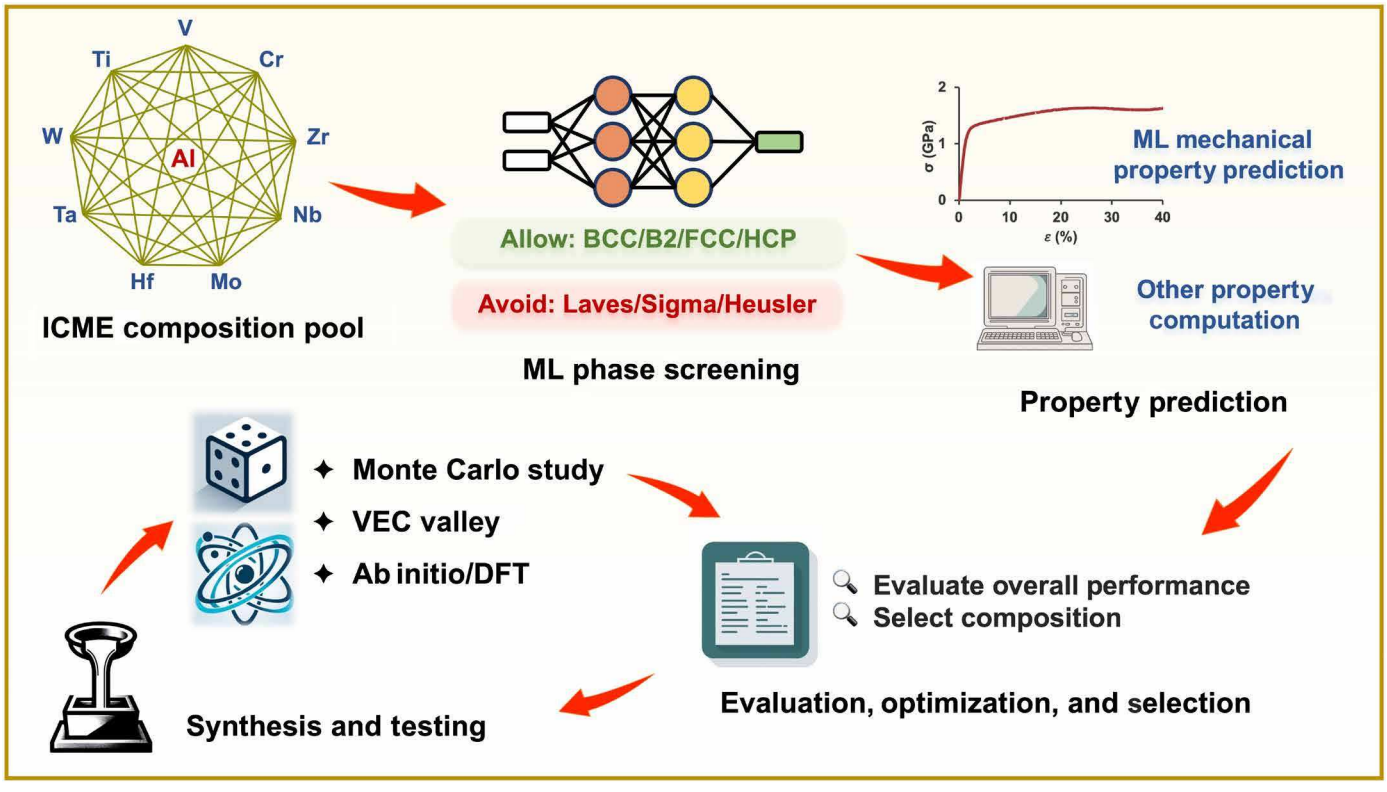

Fig. 1. Schematic diagram showing the Al-RHEAs design process. The abbreviations ICME, ML, VEC, and DFT denote integrated computational material engineering, machine learning, valence electron count, and density functional theory, respectively.

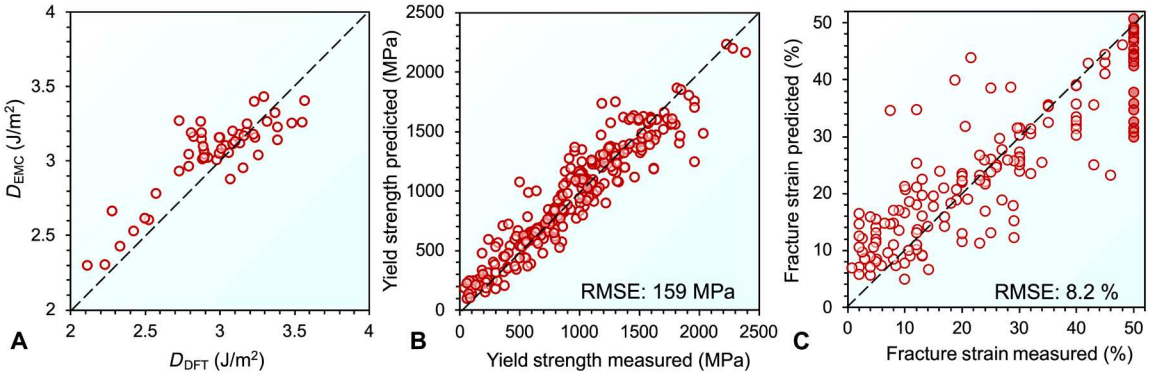

D

Alloy	ε_f (%)	σ_{YS} (MPa)	T_{melt} (K)	$\bar{\nu}$	Score
$Al_{25}Hf_{25}Nb_{25}Ti_{25}$	27	1206	2108	0.36	−1.19
$Al_{25}Hf_{25}Ti_{25}Zr_{25}$	27	1226	1983	0.35	−1.52
$Al_{25}Mo_{25}Ti_{25}W_{25}$	11	1080	2694	0.32	−1.87
$Al_{25}Nb_{25}Ti_{25}W_{25}$	8	1059	2606	0.34	−1.94
$Al_{25}Cr_{25}Ti_{25}W_{25}$	12	1408	2407	0.29	−1.95

Fig. 2. ML mechanical property prediction models' performances and prediction results. (**A**) Comparison of D-parameter values calculated using DFT and EMC. The EMC method demonstrates a promising agreement with DFT results, yielding an absolute mean error of 5% and validating its potential for the efficient estimation of the D parameter. (**B**) The comparison between the compressive yield strengths, σ_{YS}, as predicted by ML and measured from experiments for BCC HEAs, with an RMSE value of 159 MPa. (**C**) The comparison between the compressive fracture strain, ε_f, as predicted by ML and measured from experiments for BCC HEAs, with an RMSE value of 8.2%. The solid red data points on the right side of the figure indicate instances where compression tests terminated at a 50% strain without fracture. (**D**) The top five equimolar quaternary Al-RHEAs, predicted to form B2 phases without other IM. Their predicted properties, including σ_{YS} (yield strength), ε_f (fracture strain), T_{melt} (melting temperature), and $\bar{\nu}$ (Poisson's ratio), along with their respective scores (details in Methods), are also presented.

Al-RHEAs predominantly form an Al-X-Y B2 phase (*22*). However, owing to the limited mechanical properties data available for B2 Al-RHEAs, we alternatively develop a baseline ML model using more abundant disordered BCC RHEAs and Al-RHEAs. Because the B2 phase's LRO can introduce ordering-strengthening, enhancing strength, and reducing ductility (*29*, *31*), the baseline ML model based on BCC HEAs might underestimate strength and overestimate the ductility of B2 HEAs. Our goal is to identify Al-RHEAs with inherent ductility predicted in their BCC phase, as brittle BCC Al-RHEAs are unlikely to manifest ductility upon the formation of B2-LRO. Furthermore, 30% of the ML training database consists of HEAs with 3 to 20 atomic % (at %) Al. This Al inclusion highlights that the strengthening effect from potent Al-refractory elements bonds has been inherently considered. With the synchronized refinement of both ML algorithms and feature combinations, as elaborated in Methods, the model achieved a root mean square error (RMSE) of 159 MPa for σ_{YS}, alongside a notable alignment between the predicted and measured values, shown in Fig. 2B. The prediction of compressive ε_f exhibits a moderate RMSE of 8.2% (Fig. 2C), comparable to the leading results in similar prediction tasks (*32*). In these ML models, the prediction of ε_f is challenging primarily due to the database noise, where factors, such as sample defects (e.g., pores) and processing conditions (e.g., cooling rate and solidification direction), can greatly affect the ε_f. It is important to note that certain compression tests were terminated at 50% in instances where samples did not fracture (solid red data point in Fig. 2C). Alloys demonstrating high plasticity under these conditions were incorporated into the ML training to broaden the models' application scope. Last, with the two baseline ML models built with BCC alloys and the data challenge mentioned, we are not ambitious in obtaining precise alloy properties' predictions on B2 Al-RHEAs. The current models for σ_{YS} and ε_f exhibiting high and moderate accuracies, respectively, adequately direct us toward optimal compositional regions. These regions are then subject to further first-principles and experimental analyses and optimizations for the design of high-performance Al-RHEAs.

As depicted in Fig. 1, the ICME model begins with 84 equimolar quaternary Al-RHEAs by combining Al with any three refractory elements. The top five systems forming the B2 phase without other undesired IM, and showing the highest scores (Eq. 1), indicating the best overall properties, are listed in Fig. 2D (full list in table S4). $Al_{25}Hf_{25}Nb_{25}Ti_{25}$ emerges as the leading candidate exhibiting the best comprehensive performance, with the highest predicted ε_f (27%) and an intermediate σ_{YS} (1206 MPa) among all evaluated quaternary Al-RHEA systems assuming the absence of B2-LRO. Such plasticity surpasses many existing Al-RHEAs. However, the induction of B2-LRO is anticipated to reduce plasticity while enhancing strength. With Hf also known to enhance grain-boundary adhesion (*33*), $Al_{25}Hf_{25}Nb_{25}Ti_{25}$, is chosen for initial experimental examination. Subsequent composition adjustments for property optimization will be guided by experiments and MC studies.

MC-guided experimental optimization of Al-RHEAs $Al_{25}Hf_{25}Nb_{25}Ti_{25}$

The x-ray diffraction (XRD) and scanning electron microscopy (SEM) characterizations of the initial composition, $Al_{25}Hf_{25}Nb_{25}Ti_{25}$ in the as-cast condition, show the single–B2-phase formation (Fig. 3, A and B). This alloy exhibits high strength, with a compressive

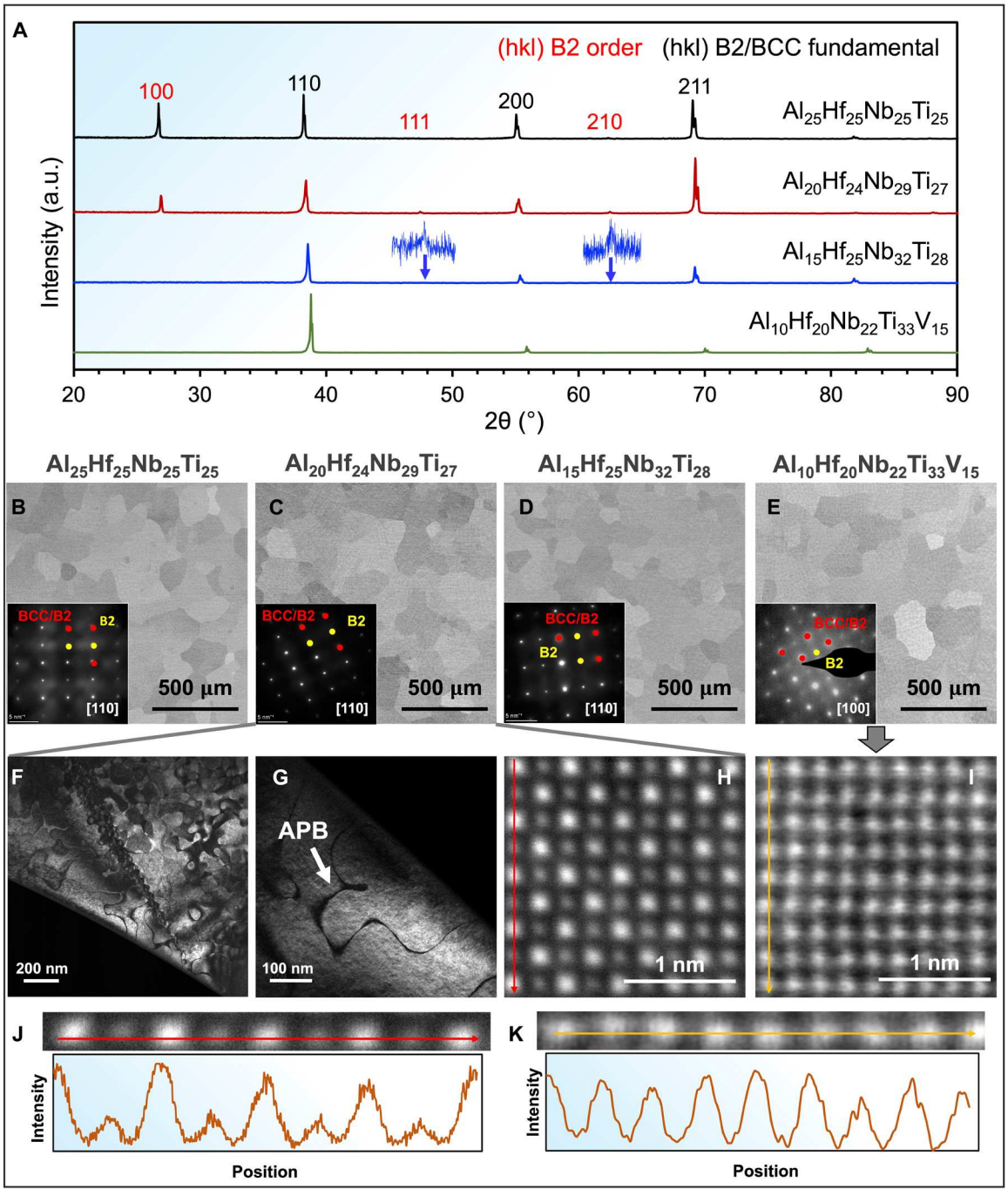

Fig. 3. Microstructures and phases for Al-RHEAs in the present work. (**A**) XRD patterns for $Al_{25}Hf_{25}Nb_{25}Ti_{25}$, $Al_{20}Hf_{24}Nb_{29}Ti_{27}$, $Al_{15}Hf_{25}Nb_{32}Ti_{28}$, and $Al_{10}Hf_{20}Nb_{22}Ti_{33}V_{33}$ in the as-cast condition. Peaks corresponding to the disordered BCC phase or B2 phase are labeled with their (hkl) indices in black or red color. For $Al_{15}Hf_{25}Nb_{32}Ti_{28}$, the insets provide higher-magnification views of the (111) and (210) superlattice diffraction peaks for the B2 phase. a.u., arbitrary units. (**B** to **E**) SEM backscattered electron (BSE) images for four alloys in the as-cast condition. B2-phase grains can be observed. Insets are the SAED showing B2-LRO. Additional SAED patterns for the four alloys, obtained from various regions of the samples, are presented in fig. S6. (**F** and **G**) TEM dark-field images for the B2 phase with an antiphase boundary (APB) in the as-cast $Al_{20}Hf_{24}Nb_{29}Ti_{27}$. (**H** and **J**) Scanning transmission electron microscopy (STEM) high-angle annular dark-field (HAADF) image for $Al_{20}Hf_{24}Nb_{29}Ti_{27}$ along the [001] zone axis. The intensity profile along the red arrow, spanning nine atoms, reveals periodic variation consistent with B2 ordering. (**I** and **K**) STEM-HAADF image for the $Al_{10}Hf_{20}Nb_{22}Ti_{33}V_{33}$ along the [001] zone axis, showing minimal variation in atomic intensity profiles due to the weak B2-LRO.

σ_{YS} ~ 1.7 GPa, but lower ε_f ~ 2% (Fig. 4A). The alloy exhibits strong B2-LRO, as indicated by the pronounced (100) superlattice XRD diffraction peak (Fig. 3A). This extensive LRO could substantially hinder dislocation movement, resulting in a higher strength but decreased plasticity, compared to the values (Fig. 2D) predicted assuming a disordered BCC phase forms.

Metropolis MC simulations (*20*, *34*) (details in Methods) were conducted to study the LRO, the B2 order-disorder transition during solidification, and the atomic sublattice occupancy. $Al_{25}Hf_{25}Nb_{25}Ti_{25}$ shows pronounced B2-LRO (Fig. 5A, LRO spans between 0 and 1, representing disordering and ordering) and atomic order parameters, LRO_i (Fig. 5C, LRO_i spans between −1 and 1, with 0 and ±1 representing disordering and ordering), with the order-disorder transformation temperature, $T_{transform}$ ~ 2000 K, slightly below the predicted melting temperature of T_{melt} ~ 2108 K by Eq. 9. Given that phase transformation and evolution in as-cast HEAs continue below T_{melt} due to high atomic kinetic energy [such a rapid phase transition may cease around 0.8 T_{melt} (*24*)], substantial B2-LRO can be developed in $Al_{25}Hf_{25}Nb_{25}Ti_{25}$ below the T_{melt}. Here, we present a semi-quantitative estimation of the LRO experimentally established in the alloy, relative to the theoretically most ordered reference state at 0 K. Specifically, the XRD patterns for the most ordered reference state were simulated using the MC structure at 0 K, and were subsequently compared with the experimentally measured XRD patterns, as detailed in Methods and Eq. 8. The LRO established in $Al_{25}Hf_{25}Nb_{25}Ti_{25}$ is estimated to be ~100% of the reference state. This estimation may suggest that a high $T_{transform}$ does exist near the T_{melt} as described earlier, facilitating LRO development. Figure 5C shows that Al and (Hf, Ti) predominantly settle to different B2 sublattices, with Nb exhibiting little inclination. The site-occupancy tendency is also evident in Fig. 5G, with Al-Ti and Al-Hf being the primary nearest-neighbor pair around Al, Hf, and Ti. Self-pairs are less prevalent in all nearest-neighbor pairs. Such site occupancy can be attributed to the binary atomic interaction energies, H_{ij}, listed in table S5, where Al-Hf and Al-Ti pairs exhibit the lowest H_{ij}, indicative of more stable bonding. Figure 5H, which shows the MC superlattice configurations at 2000, 1800, and 500 K, further illustrates the BCC-to-B2 transition. Al gradually segregates to the α sublattice, while Hf and Ti segregates to the β sublattice as temperature decreases. These MC-discovered site-occupancy preferences have been validated in similar systems like Ti_2AlHf (*35*) and AlNbTiV (*36*), by using DFT, ML, MC simulations, and experiments (*11*).

Using MC-simulated supercell structures, ab initio relaxation is used on $Al_{25}Hf_{25}Nb_{25}Ti_{25}$ (Fig. 6, A to C) to elucidate their thermodynamic phase stability at temperatures of 300, 1373, and 2000 K, corresponding to scenarios wherein LRO is either fully established, partially present, or absent, respectively. The calculated relaxation energies (ΔE) are positive, relative to the convex hull of enthalpies within the Al-Hf-Nb-Ti system, confirming that they are thermodynamically (but not dynamically) unstable to phase separation. Moreover, the decrease in quenched (0 K) ΔE from 126 meV per atom following 2000 K annealing down to 76 meV per atom following 300 K annealing demonstrates the increasing thermodynamic stability resulting from increasing chemical order. To assess the dynamic stability of the B2 structure, AIMD relaxations (Fig. 6, D to F) were conducted, wherein the $Al_{25}Hf_{25}Nb_{25}Ti_{25}$ structures were quenched from temperatures of 300, 1373, and 2000 K down to 300 K. The observed lattice distortions $<|\Delta R|>$ were of moderate magnitude, indicating the dynamic stability of the B2 phase after quenching. The extent of distortions is comparable to the Al-free RHEAs that span groups IV and V of the periodic table (*37*). The decreasing $<|\Delta R|>$ with decreasing annealing temperature suggests that LRO can reduce the lattice distortion.

The high B2-LRO substantially decreases the plasticity from the predicted ε_f value. Understanding the influence of each element on LRO is essential for the subsequent composition adjustment. Therefore, each element in $Al_{25}Hf_{25}Nb_{25}Ti_{25}$ was systematically reduced to 20 at %, generating compositions of $Al_{20}(Hf_{26.7}Nb_{26.7}Ti_{26.6})$, $Hf_{20}(Al_{26.7}Nb_{26.7}Ti_{26.6})$, $Nb_{20}(Al_{26.7}Hf_{26.7}Ti_{26.6})$, and $Ti_{20}(Al_{26.7}Hf_{26.7}Nb_{26.6})$, referred to as Al_{20}, Hf_{20}, Nb_{20}, and Ti_{20}, respectively, in Fig. 5B. $T_{transform}$ and the B2-LRO at specific reference temperatures (1500 K as an example) are calculated. Decreasing the Al content lowers both $T_{transform}$ and the B2-LRO. Conversely, reducing Hf, Nb, or Ti raises $T_{transform}$ and LRO, likely due to the resultant increase in the Al content. This trend suggests that decreasing the Al content could be a strategy to lower B2-LRO and enhance ductility/plasticity. Additional heat treatment of $Al_{25}Hf_{25}Nb_{25}Ti_{25}$ also reveals a tendency of Laves-phase formation above 700°C (fig. S1). This phase transformation does not contradict the ICME phase prediction of a single B2 formation, which is predicted for the as-cast condition. The B2 region in the as-annealed samples has an energy dispersive spectroscopy (EDS)–determined composition of $Al_{20}Hf_{24}Nb_{29}Ti_{27}$ (fig. S1). Given its thermal stability and reduced Al content, this B2 composition is chosen for a more detailed study.

$Al_{20}Hf_{24}Nb_{29}Ti_{27}$

The as-cast $Al_{20}Hf_{24}Nb_{29}Ti_{27}$ shows a single B2 phase from XRD and SEM characterizations in Fig. 3 (A and C). Transmission electron microscopy (TEM) investigations (Fig. 3, F and G) present the antiphase boundaries, with the selected area electron diffraction (SAED, inset of Fig. 3C), confirming the B2-LRO. Compression testing of $Al_{20}Hf_{24}Nb_{29}Ti_{27}$ (Fig. 4A) exhibits a σ_{YS} of 1.6 GPa, an ultimate strength of 2.4 GPa, and a notable ε_f of 35%. $Al_{20}Hf_{24}Nb_{29}Ti_{27}$ exhibits weakened B2-LRO than $Al_{25}Hf_{25}Nb_{25}Ti_{25}$, indicated by the less intense XRD superlattice diffractions and the MC studies in Fig. 5 (A and D). The MC-computed $T_{transform}$ of ~1600 K is close to 0.8 T_{melt} where a rapid phase transition still exists, allowing for substantial B2-LRO development. It is estimated that ~85% (Eq. 8) of the LRO for the reference state at 0 K is established. Al and (Hf,Ti) continue their sublattice segregation (Fig. 5D and fig. S2). Scanning transmission electron microscopy (STEM) high-angle annular dark-field (HAADF) images in Fig. 3 (H and J) also reveal the distinct periodic variations in the intensity profile for $Al_{20}Hf_{24}Nb_{29}Ti_{27}$, consistent with B2 ordering. These periodic variations are more clearly visible in the lower-magnification STEM-HAADF image shown in fig. S7. $Al_{20}Hf_{24}Nb_{29}Ti_{27}$ exhibits a substantial ε_f improvement, about 16 times that of $Al_{25}Hf_{25}Nb_{25}Ti_{25}$, with nearly unchanged σ_{YS}. This feature improved plasticity, which could be attributed to the moderated B2-LRO, facilitating plastic deformation through the glide of either <111> or a/2 <111> dislocations (*38*). The LRO decrease does not notably affect the overall strength. Next, a further Al reduction, as in $Al_{15}Hf_{25}Nb_{32}Ti_{28}$ with other elemental contents increased accordingly, may decrease the LRO and facilitate plasticity increase.

$Al_{15}Hf_{25}Nb_{32}Ti_{28}$

The as-cast $Al_{15}Hf_{25}Nb_{32}Ti_{28}$ exhibits a single B2 phase (Fig. 3D) with weak B2-LRO indicated by the magnified B2-(111) and (210) peak in the inset of Fig. 3A. TEM-SAED (Fig. 3H) further confirms

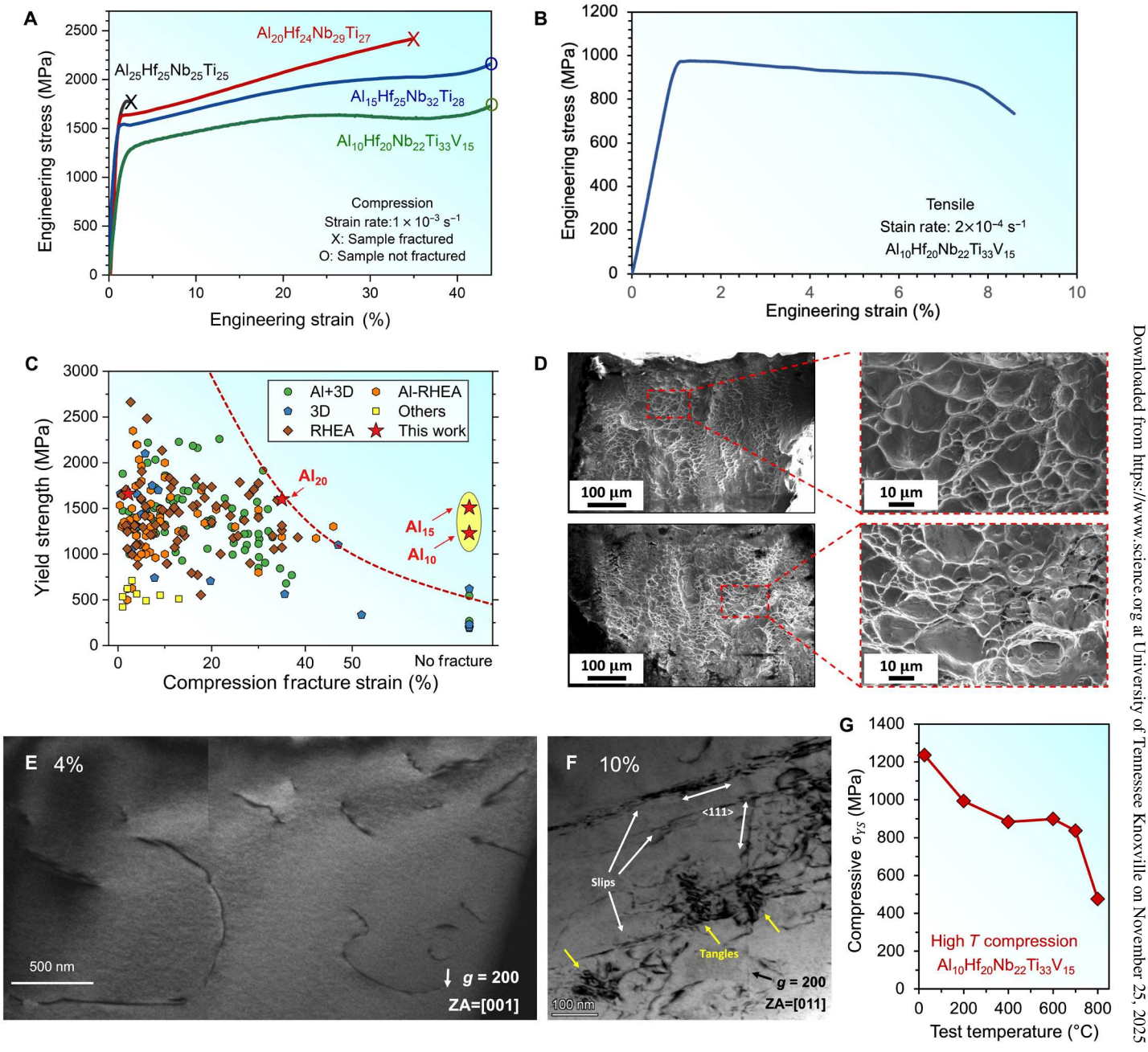

Fig. 4. The mechanical properties of Al-RHEAs in the present work. (**A**) Representative compression engineering stress-strain curves for the as-cast $Al_{25}Hf_{25}Nb_{25}Ti_{25}$, $Al_{20}Hf_{24}Nb_{29}Ti_{27}$, $Al_{15}Hf_{25}Nb_{32}Ti_{28}$, and $Al_{10}Hf_{20}Nb_{22}Ti_{33}V_{33}$. Tests terminated with the sample fractured are labeled by crosses, while circles represent nonfractured samples. (**B**) Representative tensile engineering stress-strain curves for the as-cast $Al_{10}Hf_{20}Nb_{22}Ti_{33}V_{33}$. (**C**) Comparison of the compressive yield stress and fracture strain among HEAs in different categories; 3D represents HEAs with only 3D-transition metals. RHEAs denote HEAs with only refractory elements. Al+ represents the inclusion of Al. The two alloys in the present work with high toughness are highlighted with yellow oval. (**D**) SEM images showing the ductile fracture surfaces of an $Al_{10}Hf_{20}Nb_{22}Ti_{33}V_{33}$ tensile test specimen. (**E**) TEM image of the 4% plastic-strained $Al_{10}Hf_{20}Nb_{22}Ti_{33}V_{33}$ sample, showing discrete long curved dislocations. The vertical boundary in the image results from the stitching of two TEM images. (**F**) TEM image of the 10% plastic-strained $Al_{10}Hf_{20}Nb_{22}Ti_{33}V_{33}$ sample, where multiple slip systems are observed, with the corresponding slip bands intersecting each other. (**G**) High-temperature compression test showing the variation of the compressive yield strength against test temperature for the $Al_{10}Hf_{20}Nb_{22}Ti_{33}V_{33}$.

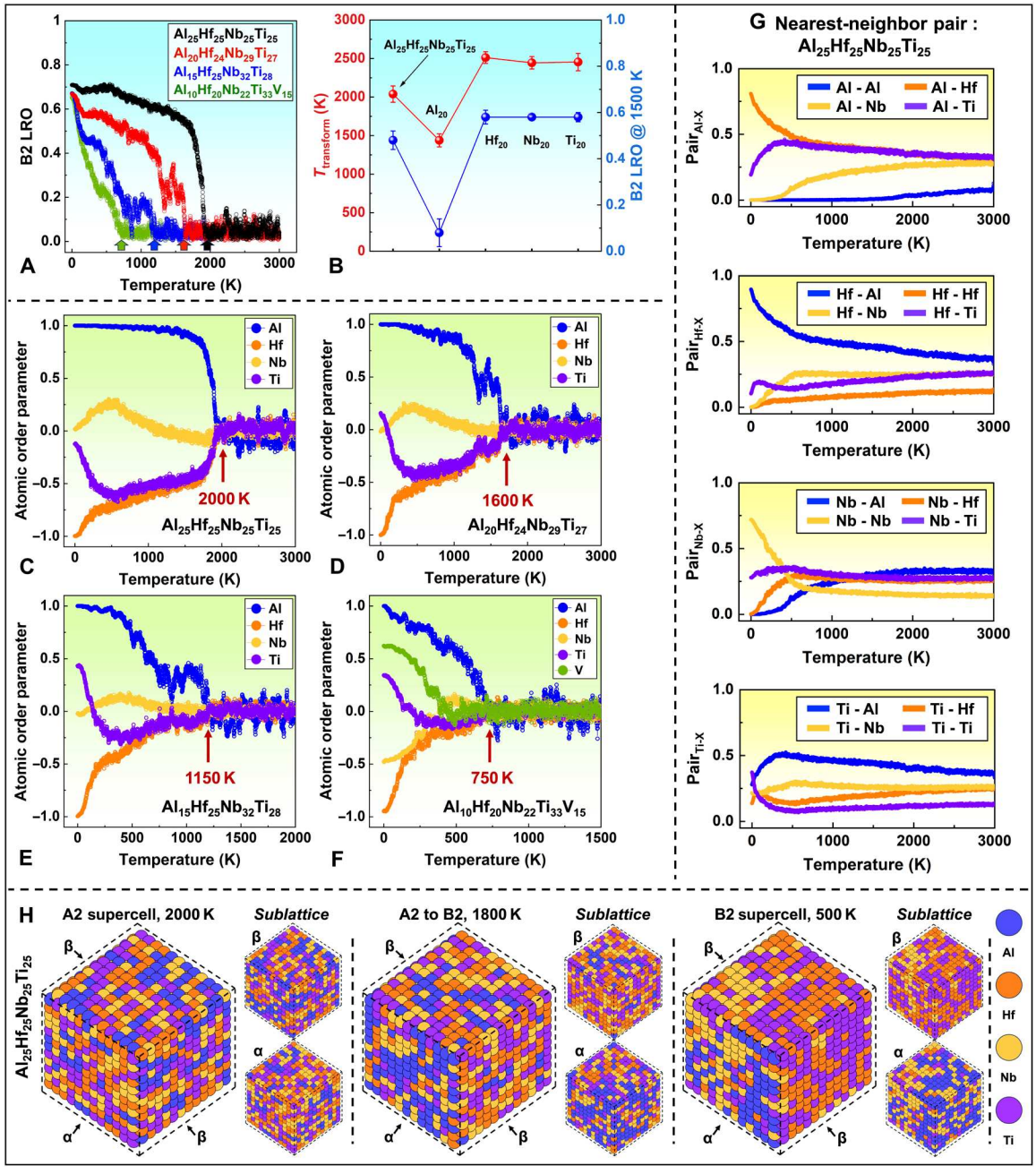

Fig. 5. Metropolis MC simulation results for Al-RHEAs. (**A**) Variation of LRO of the B2 phase under different temperatures in the four alloys: $Al_{25}Hf_{25}Nb_{25}Ti_{25}$, $Al_{20}Hf_{24}Nb_{29}Ti_{27}$, $Al_{15}Hf_{25}Nb_{32}Ti_{28}$, and $Al_{10}Hf_{20}Nb_{22}Ti_{33}V_{15}$ represented by black, red, blue, and green lines, respectively. LRO spans between 0 and 1, representing disordering and ordering. The temperatures where B2-LRO disappears are labeled. (**B**) Variation of B2-ordering transformation temperature, $T_{transform}$, and B2-LRO at 1500 K with different compositions. Al_{20}, Hf_{20}, Nb_{20}, and Ti_{20} represent $Al_{20}(Hf_{26.7}Nb_{26.7}Ti_{26.6})$, $Hf_{20}(Al_{26.7}Nb_{26.7}Ti_{26.6})$, $Nb_{20}(Al_{26.7}Hf_{26.7}Ti_{26.6})$, and $Ti_{20}(Al_{26.7}Hf_{26.7}Nb_{26.6})$, respectively. Error bars are from the SDs of five rounds of MC calculations. (**C** to **F**) Variation of atomic order parameters, LRO_i, under different temperatures for $Al_{25}Hf_{25}Nb_{25}Ti_{25}$, $Al_{20}Hf_{24}Nb_{29}Ti_{27}$, $Al_{15}Hf_{25}Nb_{32}Ti_{28}$, and $Al_{10}Hf_{20}Nb_{22}Ti_{33}V_{15}$. LRO_i spans between −1 and 1, with 0 and ±1 denoting disordering and ordering, respectively. (**G**) Variation of nearest-neighbor pair for different elements under various temperatures for $Al_{25}Hf_{25}Nb_{25}Ti_{25}$. (**H**) The atomic configurations of the MC-simulated superlattices at temperatures of 2000, 1800, and 500 K, illustrating the transition from the disordered BCC (A2 phase) to partially ordered, and fully ordered B2 within the $Al_{25}Hf_{25}Nb_{25}Ti_{25}$ system. Two small cubes at each temperature denote the α and β sublattices of the B2-lattice structure, showing the sublattice elemental segregation tendency.

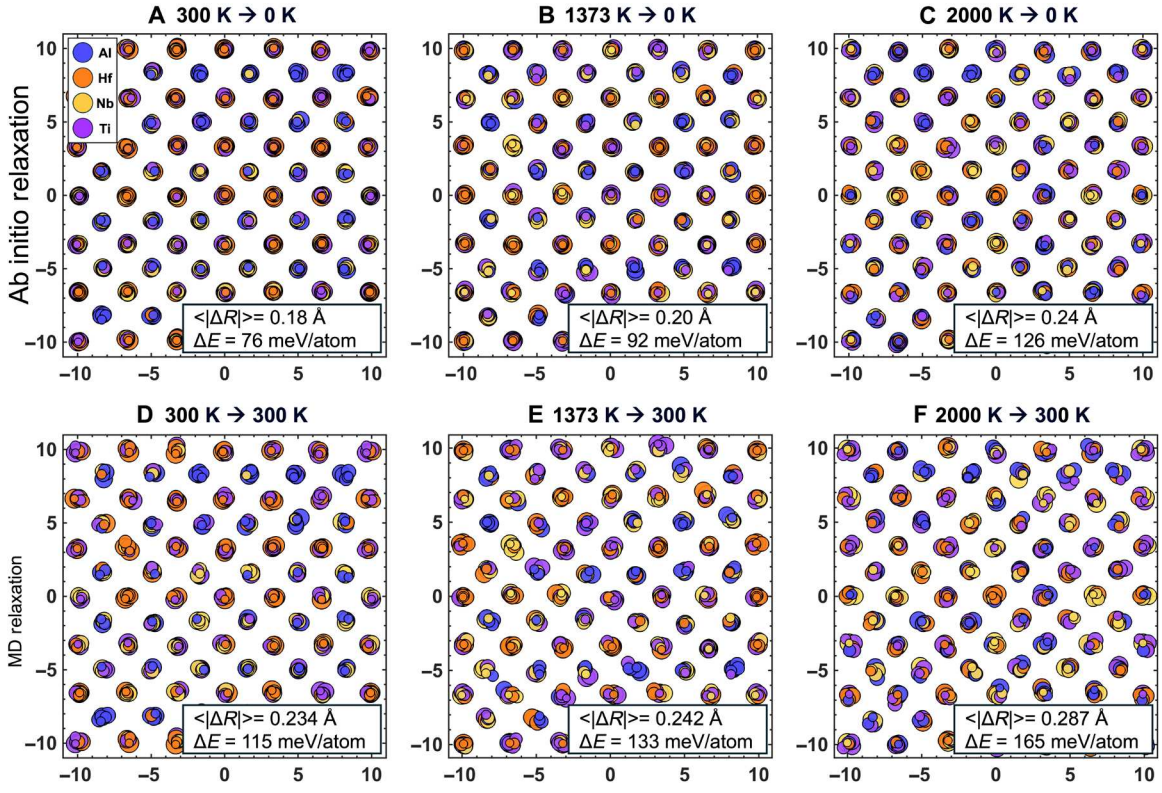

Fig. 6. Supercells of $Al_{25}Hf_{25}Nb_{25}Ti_{25}$ after ab initio relaxation and AIMD simulations. (**A** to **C**) Ab initio relaxation of $Al_{25}Hf_{25}Nb_{25}Ti_{25}$, starting from MC-determined supercell at (A) 300 K, (B) 1373 K, and (C) 2000 K. (**D** to **F**) AIMD simulations for the $Al_{25}Hf_{25}Nb_{25}Ti_{25}$ at 300 K, quenched from an MC-determined supercell (D) at 300 K, (E) 1373 K, and (F) 2000 K. The axes represent the Cartesian coordinates of each atom in angstroms. The atoms size indicates their vertical height. The calculated relaxed lattice distortions, $<|\Delta R|>$ (defined in the Methods section), and the relaxed energies, ΔE, are included for each structure.

the B2-LRO. The compression test (Fig. 4A) exhibits a σ_{YS} of 1.5 GPa. Notably, the samples endured up to a 50% height reduction without fracture before the test termination, demonstrating exceptional plasticity.

Compared to $Al_{25}Hf_{25}Nb_{25}Ti_{25}$ and $Al_{20}Hf_{24}Nb_{29}Ti_{27}$, $Al_{15}Hf_{25}Nb_{32}Ti_{28}$ experiences a marginal σ_{YS} reduction by ~ 10%, but a notable ε_f increase. Concurrently, B2-LRO is further weakened to be nearly XRD undetectable, suggesting that LRO exerts a more pronounced effect on plasticity rather than strength. The MC studies in Fig. 5 (A and E) show a $T_{transform}$ of ~1150 K, around half of the predicted T_{melt} of ~2208 K. The limited atomic mobility and diffusion at $T_{transform}$ lead to only a minimal LRO establishment, estimated to be ~33% of the reference state at 0 K.

$Al_{10}Hf_{20}Nb_{22}Ti_{33}V_{15}$

We demonstrated that an Al reduction in the AlHfNbTi system reduces B2-LRO, improving plasticity and slightly reducing strength. While pursuing a further Al reduction, we also explored partially substituting Hf with V. Vanadium has a high Poisson's ratio among the refractory elements, and with benefits of lower density and cost. The inclusion of V is predicted to maintain a single B2 phase. In addition, vanadium exhibits a moderate binary mixing enthalpy with Al (table S5), suggesting a potential substitution of strong Al-Hf bonds with weaker Al-V bonds, which may contribute further to the reduction of LRO. This strategic compositional modification has resulted in the development of $Al_{10}Hf_{20}Nb_{22}Ti_{33}V_{15}$, a stable single B2-phase alloy exhibiting both compression plasticity and tensile ductility.

The XRD and SEM characterizations (Fig. 3, A and E) reveal a single phase, and the B2-LRO is observable in the TEM-SAED (inset of Fig. 3E and fig. S6). The compression test (Fig. 4A) yields a σ_{YS} of 1.2 GPa, with no fracture up to 50% height reduction, aligning with the reduced B2-LRO leading to lower strength but more plasticity. High-temperature compression tests (Fig. 4G) maintain σ_{YS} above 800 MPa at 700°C, with a rapid strength decline around 800°C. The tensile test (Fig. 4B) exhibits a σ_{YS} of 1.0 GPa and ε_f of 9%, with tensile fracture surfaces (Fig. 4D) further substantiating the ductility. Herein, to the best knowledge of the authors, the current alloy is the first instance of a single B2 phase Al-RHEA alloy exhibiting 9% tensile ductility in the as-cast condition. While several disordered BCC RHEAs with excellent ductility (10 to 20%) have been reported in recent years (*2*), our findings challenge the assumption that B2 LRO inherently compromises ductility, thereby making the observed tensile ductility in a single B2 Al-RHEA a notable achievement. Continued research efforts into mechanical and thermal treatments are anticipated to refine the microstructure and further enhance the ductility of the alloy, though such investigations fall beyond the scope of this article and will not be further discussed. Further TEM analysis was performed at 4 and 10% strains. At a 4% strain (Fig. 4E), discrete long dislocations with the curved morphology are observed. Such morphology likely indicates dislocation pinning resulting from the chemical ordering of the B2 phase, which contrasts with the

typical straight dislocations commonly seen in BCC RHEAs (*39*). At a 10% strain (Fig. 4F), there is a noticeable increase in dislocation density and dislocation-dislocation interaction. Multiple slip systems along <111> are activated, with intersecting slip bands (white arrows) and frequent dislocation tangles (yellow arrows). The activation of multiple slip systems is hypothesized to contribute to the high plasticity/ductility observed in these alloys.

In addition, what captures our attention is the relatively low strain hardening in the tensile plastic region (Fig. 4B). A hypothesis for this phenomenon is that an intriguing yet often overlooked factor influencing the disordered BCC-B2 transformation is strain or deformation. For example, a 50% compression reduction in $AlNbTiVZr_{0.5}$ results in the loss of B2 LRO and a B2-to-disordered BCC transformation (*11*). Systems with lower LRO are more prone to such transformations (*11*). Deformation processes, including dislocation glide, annihilation, and recovery, can alter atomic arrangements and disrupt long-range atomic ordering (*40*). In our alloy, it is likely that as soon as the material enters the plastic region, the formation and movement of dislocations reduce the LRO. This reduction in LRO would inevitably diminish the LRO-strengthening effect, making subsequent dislocation movement easier and reducing the strain-hardening effect. This hypothesis presents an intriguing mechanism for balancing strength and ductility: Before permanent damage occurs, the B2 LRO provides a higher yield stress. However, once the material undergoes permanent plastic deformation, the automatic reduction in B2 LRO could help prevent early failure, as seen in most strong but brittle materials. However, such plausible emphasis needs experimental verification, such as the in situ neutron diffraction.

The MC results (Fig. 5, A and F) show a $T_{transform}$ of ~750 K, markedly below the predicted T_{melt} of ~2058 K. Nonetheless, the $Al_{10}Hf_{20}Nb_{22}Ti_{33}V_{15}$ manifests a faint B2 ordering, likely attributable to the restrained yet present atomic mobility around $T_{transform}$. Such a faint B2 LRO is obscured by the XRD background noise and can only be resolved by TEM. Correspondingly, STEM-HAADF images in Fig. 3 (I and K) exhibit minimal atom intensity variation. The unobservable and observable weak B2 ordering noted in the two methods (XRD and TEM) can be attributed to the difference in scattering factors using x-ray and electron beam. An MC study shows that Al and Hf segregate to different sublattices, while the Nb and V exhibit weak superlattice occupancy tendencies when cooling to slightly below $T_{transform}$ (~750 K, Fig. 5F). A further temperature decline below 500 K leads to pronounced elemental segregation driven by the nominal impact of entropy. However, this low-temperature region is less important as achieving the MC-predicted equilibrium state is nearly impossible given the exceptionally sluggish atomic diffusion.

Comparative study of Al-RHEAs' mechanical properties

Around 200 HEAs are compared for compressive σ_{YS} and ε_f in Fig. 4D, with the red line highlighting the trend of increased strength with decreased plasticity. Most Al-RHEAs exhibit limited plasticity, potentially due to the alloy's inherent brittleness (*41*), as elaborated in the next section; strong Al-induced B2-LRO; and brittle IM formation (*11*, *13*). However, Al-RHEAs designed in the present work diverge from this norm, achieving both high strength and plasticity/ductility. These ICME-designed Al-RHEAs exhibit inherent ductility and avoid brittle IM formation. Subsequent experimental MC hybrid optimizations are applied to adjust the LRO, thereby enhancing the plasticity/ductility of the alloy without compromising its strength.

VEC valley of metal brittleness and DFT analysis

During the ICME ML training process, we identified an intriguing correlation between VEC (*21*) and HEA plasticity. Figure 7A shows a "VEC valley" of brittleness between 5.5 and 6.2 in graph plotting compressive σ_{YS} against VEC. This valley is not attributed to data deficiency, as we specifically targeted HEAs in this VEC range. Previous ML studies (*42*, *43*) have recognized the strong VEC-plasticity/ductility correlations, and the D parameter, known to indicate plasticity/ductility, also correlates with VEC (*29*, *30*). Notably, our Al-RHEAs are consistently located in the lower-VEC regions, outside the valley, where high-plasticity/ductility HEAs are typically found.

Empirical studies (*21*) suggest a "spectrum" of the VEC-HEA phase formation, where VEC < 6 favors BCC formation, 6 < VEC < 7.8 leads to a mixed FCC-BCC phase, and VEC > 7.8 leads to a single FCC phase. The range, 6.88 < VEC < 7.84, tends to form brittle

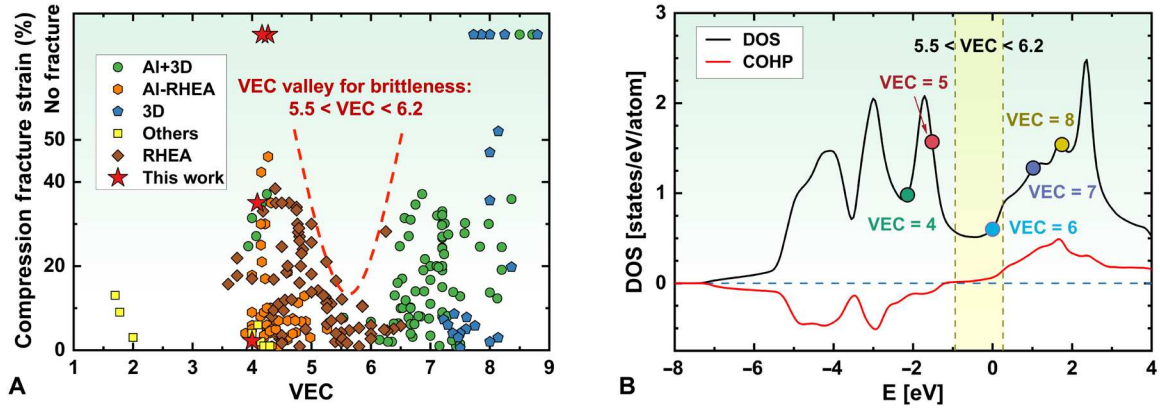

Fig. 7. The VEC valley for alloy brittleness and its DFT explanation. (**A**) Comparison of the compressive fracture strain and VEC among HEAs in different categories. In both figures, 3D represents HEAs with only 3D-transition metals. RHEAs denote HEAs with only refractory elements. Al+ represents the inclusion of Al. The four alloys in the current work are highlighted by the star symbol. (**B**) The DOS of Mo (black line) showing the variation of $D(E_F)$ with respect to the VEC in a rigid-band model. Plotting symbols are placed at energies corresponding to VECs of the periodic table columns 4 to 8 (Ti-Fe columns). The Fermi energy for VEC = 6 is set to zero. The brittle region (5.5 < VEC < 6.2) is shaded. The crystal orbital Hamiltonian population (COHP) (*50*) is plotted in the red curve. The negative and positive COHP values indicate bonding and antibonding states, respectively.

topologically close-packed (TCP) phases (e.g., Laves and Sigma) (*44*). The VEC valley resides near the higher BCC and mixed FCC-BCC regions, close to the brittle TCP region. To the right of the valley, HEAs typically form ductile FCC phases, while to the left, they form ductile BCC phases. A decreasing VEC lowers the Fermi level in the band structure, leading to an earlier occurrence of the critical strain for shear instability and thus inherently enhancing the plasticity/ductility (*41*). Therefore, the VEC valley only occupies the higher end of the BCC region.

Beyond these reasons, a more in-depth, quantitative analysis is critical for deciphering the fundamental mechanisms that underpin this phenomenon, and DFT was applied to provide more insight. Prior studies (*45*, *46*) suggest that the Fermi level density of states, $D(E_F)$, correlates with plasticity/ductility due to the strength of metallic bonding relative to ionic and covalent bonds. Other work has linked high plasticity/ductility to incipient shear instabilities governed by the proximity of the Fermi level to topologically unstable energy-band crossings (*47*, *48*). Electronic-structure effects may thus help explain the non-monotonic variation of fracture strain with respect to VEC. Figure 7B presents $D(E)$ for a representative refractory metal, BCC Mo, with VEC = 6 at the center of the experimental region of interest. The pronounced pseudogap around the Fermi level at $E_F = 0$ is caused by the $E_g - T_{2g}$ splitting at the Γ k-point with the Mo d-band half-filled in its standard electron configuration, $5s^1 4d^5$. In a rigid band model (*49*), we may assume that $D(E)$ for the alloys under study qualitatively resembles that of Mo, with the chief difference (other than the possible magnetism) being the placement of the Fermi level, which grows monotonically with VEC. The VEC valley for brittleness (Fig. 7B) roughly coincides with the region of relatively low $D(E_F)$. Moreover, as demonstrated by the crystal orbital Hamilton population (COHP, Fig. 7B) (*50*), the $E_g - T_{2g}$ split that creates the deep pseudogap separates occupied bonding states (negative COHP) from antibonding (positive COHP). The Fermi level for Mo lies in this gap, and thus the valley represents the maximum degree of covalency in the bonding. Covalent bonds create strong shear moduli that lower the Poisson ratio, contributing to brittleness. Besides, the Thomas-Fermi screening length varies as $1/\sqrt{D(E_F)}$. Therefore, a low $D(E_F)$ corresponds to a large screening length. Al-transition metal alloys are subject to strong charge transfer that, together with the large screening length, makes the bonding more ionic in character. Last, we want to remind the reader that the avoidance of the VEC valley is potentially a necessary condition, but not a sufficient condition for locating ductile HEAs. As can be seen from Fig. 7A, many HEAs outside the VEC valley still exhibit low ductility due to factors, such as unfavored IM formation.

In addition, we calculated the $D(E_F)$ for the alloys in this study using MC supercells at 500 K and 2500 K (Table 1), corresponding to ordered and disordered atomic distributions, respectively. The DFT explanations for the VEC valley of brittleness are again applicable: The steadily decreasing $D(E_F)$ values with increasing Al content seem to suggest a correlation with plasticity, as discovered in other metallic systems (*45*). The B2 ordering appears to have minimal impact on the $D(E_F)$, except in the case of $Al_{25}Hf_{25}Nb_{25}Ti_{25}$. This is likely because all alloys in this study are substantially distant from the 50% of the Al fraction, where strong pseudogaps are typically observed in alloys containing late transition metals, such as Al-Mn through Al-Ni (*51*).

DISCUSSION

HEAs offer a remarkable latitude in designing alloys with multiple promising properties. This potential, however, brings the complex challenge of systematically exploring the HEA compositional space for optimal compositions suitable for various applications. The past decade has witnessed a surge in the HEA-phase prediction research (*26*), and recognized ML and CALPAHD as ideal computational tools for high-throughput computation. Concurrently, many models for predicting properties emerged with high accuracies (*42*, *43*, *52*), paving the way for the inception of all-encompassing ICME HEA design models. The discovery of the strong, yet ductile Al-RHEAs epitomizes a refined template model, and the ICME framework and submodels can be customized accordingly to divergent design objectives. While ICME effectively identifies promising compositional zones, it is ambitious to rely on it alone in a multiobjective quest to determine the optimal composition. As shown with the AlHfNbTi(V) system, fine-tuning the composition necessitates deeper theoretical analysis, such as MC and DFT, complemented by experimental validation and refinement.

To review the AlHfNbTi(V) system, four B2 Al-RHEAs were designed with plasticity primarily determined by B2-LRO and adjustable through the Al content. MC studies suggest that the LRO may also be modulated through specific thermal treatments, tailoring ductility for specific applications. Notably, AlHfNbTi(V) alloys demonstrate toughness surpassing most extant HEAs, with the Al incorporation effectively reducing cost and density while enhancing oxidation resistance, positioning this system as promising for continued optimization and research.

Regarding the fundamental mechanism of the VEC-plasticity correlation, first-principles calculations have elucidated an electronic origin of the VEC valley. A more in-depth investigation is imperative, propelling the field toward an enriched understanding of electronic structure effects on alloy ductility. Concurrently, strategically avoiding the VEC valley is advised in designing future ductile alloys.

Table 1. $D(E_F)$ calculated using the MC structure at 500 and 1500 K for alloys in the present work.

Composition	$D(E_F)$—500 K (states per electron volt per atom)	$D(E_F)$—2500 K (states per electron volt per atom)
$Al_{10}Hf_{20}Nb_{22}Ti_{33}V_{15}$	1.36	1.34
$Al_{15}Hf_{25}Nb_{32}Ti_{28}$	1.21	1.20
$Al_{20}Hf_{24}Nb_{29}Ti_{27}$	1.13	1.15
$Al_{25}Hf_{25}Nb_{25}Ti_{25}$	1.00	1.10

Moving ahead, we envision this innovative alloy-design strategy as a blueprint for designing alloys with structural applications. We also aim to deepen understanding of the elemental role in the atomic ordering and mechanical properties in HEAs and explore VEC-centric compositional tuning to overcome brittleness, thereby perfecting the approach and enriching the theoretical framework.

METHODS

EMCs of D parameter

The D parameter quantifies the ratio between the surface energy associated with the cleavage fracture (γ_{sf}) and the energy associated with the unstable stacking fault (γ_{usf}) (*29*). A distinct correlation has been observed between the compression fracture strain and the DFT-calculated D parameter for BCC HEAs (*29*) because it has been postulated that the ductility of BCC alloys is influenced by the interplay between the dislocation emission and cleavage-fracture propagation in the vicinity of a crack tip (*30*). Despite its importance, the D parameter computed by DFT is computationally expensive and not suitable for high-throughput simulations. Alternatively, in our effective medium method (*28*), the D parameter is calculated by considering the values of surface energies and unstable stacking fault energies along the same atomic planes and dislocation directions for each constituent element with the equation and details listed in table S1.

ML mechanical properties and phase-formation prediction model

The ML mechanical property prediction database includes 272 compressive yield strength (σ_{YS}) and 157 compressive fracture strain (ε_f) measurements measured at both ambient temperature and elevated temperatures up to 1600°C. The complete ML feature set is listed in table S1, where the T_{test}/T_{melt} feature, the testing temperature relative to melting temperature, highlights the effect of testing temperature on material properties. Feature selection will be refined from this set. Several ML algorithms, including the support vector regressor, random forest regressor (RFR), K-nearest neighbor, and linear regression, were applied to the σ_{YS} and ε_f datasets, using the Python's scikit-learn library. The GA (*27*) (GA parameters in table S3) was used for the optimal feature selection from the complete feature set (table S1). The GA process used the 10-fold cross-validation for overfitting avoidance and GridSearchCV() for hyperparameter optimization, identifying RFR as the best algorithm for both σ_{YS} and ε_f predictions with the lowest prediction RMSE. The GA-determined optimal feature combinations are included in table S2.

The ML-phase formation prediction models are detailed in our prior work (*24*, *25*).

ICME alloy system selection

Of the 84 equimolar quaternary Al-RHEAs, 16 Al-RHEAs systems are screened out by the ML prediction of forming the B2 phase without other IMs. These systems are then predicted for the compressive σ_{YS}, ε_f, T_{melt} (Eq. 9), and $\bar{\nu}$ (equation in table S1). Three heavier Al-RHEAs, with ρ exceeding 10 g/cm^3, are excluded due to their notably higher density, compared to Ni- and Co-based superalloys. The predicted property values for each system are summarized in table S4. Each alloy is scored using

$$\text{score} = \sum_{\text{all } i} \frac{p_i - p_{i-\text{best}}}{p_{i-\text{range}}} \quad (1)$$

where p_i represents the predicted value of the ith property for the alloy, $p_{i-\text{best}}$ and $p_{i-\text{range}}$ are, respectively, the best value (i.e., the highest ε_f, σ_{YS}, T_{melt}, and $\bar{\nu}$) and the range for the ith property among all the candidates. A higher score represents a better overall performance.

Experiment methods

High-purity raw elements (>99.99 wt %) were arc melted in a water-cooled copper crucible using a 400-A current. Each melt lasted 30 s, with at least five melts performed to ensure chemical homogeneity, and the ingots were flipped between each melt. The ingots were later polished for XRD and SEM analysis. Parts of the ingots were also suction-cast into copper molds to produce a rod-shaped sample (3 mm diameter and 10 mm height) for compression testing and TEM sample preparation.

The XRD/SEM samples were polished down to a grit size of 1 μm with diamond suspension and finished with a 0.06-μm colloidal silica suspension. The TEM samples were sliced from the suction-cast rod with a thickness of 500 μm. These thin slices were further polished to a thickness below 100 μm, followed by electron polishing to create TEM transparent regions for imaging.

The XRD measurements were conducted on the polished sample by a PANalytical Empyrean diffractometer with Cu Kα radiation and a scanning rate of approximately 0.15 degrees/s. The SEM characterization was conducted on an FEI Quanta 650 equipped with EDS. The TEM analysis was performed, using an FEI Titan Transmission Electron Microscope and a Thermo Scientific Spectra 300 (S)TEM with an accelerating voltage of 200 kV.

Cylindrical samples with a diameter of 3 mm and a gauge length of 6 mm were used for compression testing. Compression tests were performed on a computer-controlled, uniaxial-mechanical testing system (an MTS servo-hydraulic load frame) with an initial strain rate of 1×10^{-3} s^{-1}. The load and displacement values of the testing system were recorded without specimens, and these displacement values were subtracted from the measured displacement values in compression tests at their corresponding load. This method excludes the elastic responses of the load frame, load cell, and sample grips. Then, the deformation of the specimens could be calculated. Tensile samples with a gauge length of 2 cm were cut from the arc-melted ingots by electrical discharge machining. Tensile tests were conducted on a computer-controlled, uniaxial mechanical testing system (an MTS servo-hydraulic load frame) with an initial strain rate of 2×10^{-4} s^{-1}. The strain values were recorded with an attached extensometer.

Density functional theory

The first-principles calculations were performed within the electronic DFT (*53*, *54*), using the Vienna Ab initio Simulation Package (VASP) code (*55*, *56*) in the Perdew-Burke-Ernzerhof generalized gradient approximation (*57*). Atomic coordinates and lattice parameters were relaxed with a high k-point density and default plane-wave energy cutoff. The Mo density of states (DOS) was calculated, using tetrahedron integration with a subsequent 0.1 eV Gaussian smearing, and we have shifted the energy scale to place the Fermi energy of Mo at zero. Fermi energies for VEC = 4 to 8 were calculated from the integrated density of states. The COHP (*50*) was calculated using the

LOBSTER code (*58*) to determine the energy-dependent contributions of the interatomic bonding to the total energy. The negative and positive COHP values indicate bonding and antibonding states, respectively. Electronic orbitals were calculated using VASP (*55*, *56*) and the Mo 4p, 4d, and 5s atomic orbitals were used in the projection. Values of COHP are dimensionless, and the integral up to the Fermi energy yields an energy related to the bond strength.

AIMD simulations and relaxations were performed for 6 × 6 × 6 supercells of 432 atoms at the equiatomic composition. A single k-point was used in these calculations. AIMD simulations were in the NVT ensemble at the temperatures indicated for a duration of 500 fs using 1-fs time steps. Conjugate gradient relaxations were performed until the maximum forces fell below 0.01 eV/Å.

After relaxation, the mean atomic displacement, representing the lattice distortion is defined as

$$<|\Delta R|> = \frac{\sum_{\text{all } k} |\overrightarrow{\mathbf{R_k}} - \overrightarrow{\mathbf{R_{k-0}}}|}{N} \quad (2)$$

Here, $\overrightarrow{\mathbf{R_{k-0}}}$ and $\overrightarrow{\mathbf{R_k}}$ are the Cartesian coordinates of the atom, *k*, before and after relaxation. $|\overrightarrow{\mathbf{R_k}} - \overrightarrow{\mathbf{R_{k-0}}}|$ represent the magnitude of the atomic-displacement vector. *N* is the total number of atoms in the supercell.

Electronic densities of states were calculated for simulated structures of 432 atoms in a 6 × 6 × 6 BCC supercell. The structures were fully relaxed in position and lattice parameters using the electronic DFT with standard pseudopotentials and a single electronic k-point. The density of state was then calculated for the relaxed structure using a 2 × 2 × 2 k-point mesh.

MC simulation

The Metropolis MC simulation (*20*, *34*) incorporates the nearest-neighbor interaction paradigm with the nearest-neighbor interaction energy, v_{ij}, given by

$$v_{ij} = \frac{H_{ij}}{z} \quad (3)$$

Here, H_{ij} is the binary energy of formation (*59*). The parameter *z* is the number of the nearest-neighbor bonds per atom and has a value of 4 in the BCC structure (*20*). H_{ij} values used in this study are tabulated in table S5.

The system commences with a randomized structural configuration, mirroring the disordered alloy's atomic disposition. Within every MC iteration, a random change to the current configuration is proposed. Here, this random alteration is the positional exchange of two atoms. The energies of the old and the modified configurations are compared. If the modified configuration has lower energy, it is accepted. If it has higher energy, it is accepted with a Boltzmann probability, *P*

$$P = e^{\frac{-\Delta H}{k_B T}} \quad (4)$$

where ΔH is the energy difference between the two configurations, k_B is the Boltzmann constant, and *T* is the temperature. The MC simulation in this study uses a configuration of a 12 × 12 × 12 supercell of the BCC unit cell comprising 3456 atoms and executes more than 10^7 MC iterations.

The BCC/B2 lattice comprises two distinct sublattices, α and β. In a disordered BCC phase, elements are uniformly distributed between α and β, while in an ordered B2 matrix, they show sublattice preference. The order parameter for atom *i*, denoted as LRO_i, is given by

$$\text{LRO}_i = \frac{x_{i-\alpha} - x_{i-\beta}}{x_{i-\alpha} + x_{i-\beta}} \quad (5)$$

Here, $x_{i-\alpha}$ and $x_{i-\beta}$ represent the occupancy of the element *i* on the α and β sublattices, respectively. The LRO_i value spans from −1 to 1, where 0 denotes a lack of sublattice preference. Conversely, values of 1 or −1 indicate an exclusive occupancy of a particular sublattice, representing the highest degree of atomic ordering.

The alloy's LRO is defined as

$$\text{LRO} = \sqrt{\sum_{\text{all } i} c_i \, \text{LRO}_i^2} \quad (6)$$

where c_i denotes the atomic percentage of each kind of atom, i.e., LRO spans between 0 (disordered) and 1 (ordered).

The ratio of the nearest-neighbor pairs, Pair_{i-j}, is defined as

$$\text{Pair}_{i-j} = \frac{n_{i-j}}{\sum_{\text{all } j} n_{i-j}} \quad (7)$$

within this context, $n_{i\text{-}j}$ represents the count of an atom pair, *i*-*j*, in the MC supercell. The Pair_{i-j} quantifies the probability of an atom, *j*, being among the nearest neighbors of the atom; i.e., Pair_{i-j} generally remains steady at elevated temperatures with a disordered BCC phase and is only determined by the atomic percentages of atoms *i* and *j* in the alloy. As the temperature decreases, certain nearest-neighbor pairs gain preference, leading to a deviation of the Pair_{i-j} distribution from a random arrangement. This shift underscores the dynamic nature of atomic interactions and the emerging order within the system.

The comparison of the measured XRD patterns and the simulated XRD patterns based on MC structures at 0 K with the highest B2 LRO can empirically estimate the extent of LRO in the alloy. For HEAs, stoichiometric limitations often prevent perfect lattice ordering (LRO = 1), as not every element can exclusively occupy a single sublattice. For instance, in the $Al_{15}Hf_{25}Nb_{32}Ti_{28}$, at least one element must occupy both B2 sublattices to balance atom numbers, resulting in an LRO of less than 1. A reference state is thus required for each HEA to represent the highest LRO achievable for an energetically favored atomic configuration. Herein, we select the MC-simulated supercell at 0 K as the reference state. The B2 unit cell structure parameters in each Al-RHEA's reference state can be derived from Fig. 5 (C to F) at 0 K, with detailed values listed in table S7. Powder diffraction patterns are then simulated using the VESTA (Visualization for Electronic and Structural Analysis) software (*60*), and the patterns are plotted in fig. S5. By comparing the measured XRD patterns with the reference diffraction patterns, we can estimate the extent of LRO relative to the reference state. Theoretically, the intensity of superlattice-diffraction peaks is proportional to the square of the LRO (*61*). Here, however, this rule is used only to estimate the LRO in the alloy, accounting for experimental errors from the XRD patterns obtained from the bulk material where certain favored grain growth orientations may exist. This semiquantitative evaluation on the extent of LRO developed in each alloy relative to the reference state (*S*) is expressed as

$$S^2 = \frac{I_{\text{super-measured}}}{I_{\text{super-reference}}} \quad (8)$$

Here, $I_{super-measured}$ and $I_{super-reference}$ represent the total intensities of B2-superlattice diffraction peaks in the measured XRD pattern and the powder diffraction patterns derived from the reference state, respectively. These peaks, with Miller indices of (100), (111), (210), (221), (300), and (311), are normalized by the total peak intensity in the scanned 2θ range from 20° to 110°. The range of S is from 0 to 100%, representing an alloy having no LRO to having a similar level of LRO to the reference state.

Alloy melting temperature and density prediction method

T_{melt} is predicted by the following method (*24*)

$$T_{melt} = \frac{\sum_{i \neq j} T_{i-j} \times c_i \times c_j}{\sum_{i \neq j} c_i \times c_j} \quad (9)$$

Here, $T_{i\text{-}j}$ is the binary liquidus temperature of the element pair, i-j, on the binary-phase diagram with a relative atomic ratio of c_i/c_j. The method of extracting binary liquidus temperatures is described in detail in a previous work (*24*).

The density, ρ, is predicted by the rule of mixtures

$$\frac{1}{\rho} = \sum_i \frac{w_i}{\rho_i} \quad (10)$$

Here, w_i and ρ_i are the weight percentage and density of the ith element.

Supplementary Materials

This PDF file includes:

Figs. S1 to S7
Tables S1 to S7
References

REFERENCES AND NOTES

1. D. B. Miracle, O. N. Senkov, A critical review of high entropy alloys and related concepts. *Acta Mater.* **122**, 448–511 (2017).
2. S. Wei, S. J. Kim, J. Kang, Y. Zhang, Y. Zhang, T. Furuhara, E. S. Park, C. C. Tasan, Natural-mixing guided design of refractory high-entropy alloys with as-cast tensile ductility. *Nat. Mater.* **19**, 1175–1181 (2020).
3. X. Yan, P. K. Liaw, Y. Zhang, Ultrastrong and ductile BCC high-entropy alloys with low-density via dislocation regulation and nanoprecipitates. *J. Mater. Sci. Technol.* **110**, 109–116 (2022).
4. V. Soni, B. Gwalani, O. N. Senkov, B. Viswanathan, T. Alam, D. B. Miracle, R. Banerjee, Phase stability as a function of temperature in a refractory high-entropy alloy. *J. Mater. Res.* **33**, 3235–3246 (2018).
5. V. Soni, B. Gwalani, T. Alam, S. Dasari, Y. Zheng, O. N. Senkov, D. Miracle, R. Banerjee, Phase inversion in a two-phase, BCC+B2, refractory high entropy alloy. *Acta Mater.* **185**, 89–97 (2020).
6. O. N. Senkov, D. Isheim, D. N. Seidman, A. L. Pilchak, Development of a refractory high entropy superalloy. *Entropy* **18**, 102 (2016).
7. L. Wang, J. Ding, S. Chen, K. Jin, Q. Zhang, J. Cui, B. Wang, B. Chen, T. Li, Y. Ren, S. Zheng, K. Ming, W. Lu, J. Hou, G. Sha, J. Liang, L. Wang, Y. Xue, E. Ma, Tailoring planar slip to achieve pure metal-like ductility in body-centred-cubic multi-principal element alloys. *Nat. Mater.* **22**, 950–957 (2023).
8. B. Gorr, F. Mueller, H.-J. Christ, H. Chen, A. Kauffmann, R. Schweiger, D. V. Szabó, M. Heilmaier, Development of oxidation resistant refractory high entropy alloys for high temperature applications: Recent results and development strategy, in *TMS 2018 147th Annual Meeting & Exhibition Supplemental Proceedings* (Springer International Publishing; 2018), pp. 647–659.
9. M. Li, Q. Chen, X. Cui, X. Peng, G. Huang, Evaluation of corrosion resistance of the single-phase light refractory high entropy alloy $TiCrVNb_{0.5}Al_{0.5}$ in chloride environment. *J. Alloys Compd.* **857**, 158278 (2021).
10. S. Laube, H. Chen, A. Kauffmann, S. Schellert, F. Müller, B. Gorr, J. Müller, B. Butz, H. J. Christ, M. Heilmaier, Controlling crystallographic ordering in Mo–Cr–Ti–Al high entropy alloys to enhance ductility. *J. Alloys Compd.* **823**, 153805 (2020).
11. N. Y. Yurchenko, N. D. Stepanov, S. V. Zherebtsov, M. A. Tikhonovsky, G. A. Salishchev, Structure and mechanical properties of B2 ordered refractory AlNbTiVZr$_x$ (x = 0–1.5) high-entropy alloys. *Mater. Sci. Eng. A* **704**, 82–90 (2017).
12. N. Yurchenko, E. Panina, M. Tikhonovsky, G. Salishchev, S. Zherebtsov, N. Stepanov, A new refractory Ti-Nb-Hf-Al high entropy alloy strengthened by orthorhombic phase particles. *Int. J. Refract. Met. Hard Mater.* **92**, 105322 (2020).
13. N. Y. Yurchenko, N. D. Stepanov, A. O. Gridneva, M. V. Mishunin, G. A. Salishchev, S. V. Zherebtsov, Effect of Cr and Zr on phase stability of refractory Al-Cr-Nb-Ti-V-Zr high-entropy alloys. *J. Alloys Compd.* **757**, 403–414 (2018).
14. O. N. Senkov, J. K. Jensen, A. L. Pilchak, D. B. Miracle, H. L. Fraser, Compositional variation effects on the microstructure and properties of a refractory high-entropy superalloy $AlMo_{0.5}NbTa_{0.5}TiZr$. *Mater. Des.* **139**, 498–511 (2018).
15. O. N. Senkov, C. Woodward, D. B. Miracle, Microstructure and properties of aluminum-containing refractory high-entropy alloys. *JOM* **66**, 2030–2042 (2014).
16. A. Lacour-Gogny-Goubert, Z. Zhao-Huvelin, A. Bachelier-Locq, I. Guillot, A. Denquin, Effect of Al content on microstructure and properties of Al_xMoNbTiV RCCA's alloys. *Mater. Sci. Forum* **941**, 1111–1116 (2018).
17. G. Ouyang, P. Singh, R. Su, D. D. Johnson, M. J. Kramer, J. H. Perepezko, O. N. Senkov, D. Miracle, J. Cui, Design of refractory multi-principal-element alloys for high-temperature applications. *NPJ Comput. Mater.* **9**, 141 (2023).
18. J. J. Bhattacharyya, S. B. Inman, M. A. Wischhusen, J. Qi, J. Poon, J. R. Scully, S. R. Agnew, Lightweight, low cost compositionally complex multiphase alloys with optimized strength, ductility and corrosion resistance: Discovery, design and mechanistic understandings. *Mater. Des.* **228**, 111831 (2023).
19. Z. Rao, P. Y. Tung, R. Xie, Y. Wei, H. Zhang, A. Ferrari, T. P. C. Klaver, F. Körmann, P. T. Sukumar, A. K. da Silva, Y. Chen, Z. Li, D. Ponge, J. Neugebauer, O. Gutfleisch, S. Bauer, D. Raabe, Machine learning–enabled high-entropy alloy discovery. *Science* **378**, eabo4940 (2022).
20. R. Feng, C. Zhang, M. C. Gao, Z. Pei, F. Zhang, Y. Chen, D. Ma, K. An, J. D. Poplawsky, L. Ouyang, Y. Ren, J. A. Hawk, M. Widom, P. K. Liaw, High-throughput design of high-performance lightweight high-entropy alloys. *Nat. Commun.* **12**, 4329 (2021).
21. S. Guo, C. Ng, J. Lu, C. T. Liu, Effect of valence electron concentration on stability of fcc or bcc phase in high entropy alloys. *J. Appl. Phys.* **109**, 103505 (2011).
22. D. B. Miracle, M. H. Tsai, O. N. Senkov, V. Soni, R. Banerjee, Refractory high entropy superalloys (RSAs). *Scr. Mater.* **187**, 445–452 (2020).
23. V. Soni, O. N. Senkov, J.-P. Couzinie, Y. Zheng, B. Gwalani, R. Banerjee, Phase stability and microstructure evolution in a ductile refractory high entropy alloy $Al_{10}Nb_{15}Ta_5Ti_{30}Zr_{40}$. *Materialia* **9**, 100569 (2020).
24. J. Qi, A. M. Cheung, S. J. Poon, High entropy alloys mined from binary phase diagrams. *Sci. Rep.* **9**, 15501 (2019).
25. J. Qi, D. I. Hoyos, S. J. Poon, Machine learning-based classification, interpretation, and prediction of high-entropy-alloy intermetallic phases. *High Entropy Alloys Mater.* **1**, 312–326 (2023).
26. S. J. Poon, J. Qi, A. M. Cheung, Harnessing the complex compositional space of high-entropy alloys, in *High-Entropy Materials: Theory, Experiments, and Applications*, J. Brechtl, P. K. Liaw, Eds. (Springer International Publishing, 2021), pp. 63–113.
27. F. Hussein, N. Kharma, R. Ward, Genetic algorithms for feature selection and weighting, a review and study, in *Proceedings of the International Conference on Document Analysis and Recognition, ICDAR* (IEEE; 2001), pp. 1240–1244.
28. W. P. Huhn, M. Widom, A. M. Cheung, G. J. Shiflet, S. J. Poon, J. Lewandowski, First-principles calculation of elastic moduli of early-late transition metal alloys. *Phys. Rev. B* **89**, 104103 (2014).
29. Y. J. Hu, A. Sundar, S. Ogata, L. Qi, Screening of generalized stacking fault energies, surface energies and intrinsic ductile potency of refractory multicomponent alloys. *Acta Mater.* **210**, 116800 (2021).
30. E. Mak, B. Yin, W. A. Curtin, A ductility criterion for bcc high entropy alloys. *J. Mech. Phys. Solids* **152**, 104389 (2021).
31. S. Qiu, N. Miao, J. Zhou, Z. Guo, Z. Sun, Strengthening mechanism of aluminum on elastic properties of NbVTiZr high-entropy alloys. *Intermetallics* **92**, 7–14 (2018).
32. S. A. Giles, H. Shortt, P. K. Liaw, D. Sengupta, Yield strength-plasticity trade-off and uncertainty quantification for machine-learning-based design of refractory high-entropy alloys. arXiv:2304.13932 [cond-mat.mtrl-sci] (2023).
33. Y. S. Zhao, J. Zhang, Y. S. Luo, B. Zhang, G. Sha, L. F. Li, D. Z. Tang, Q. Feng, Improvement of grain boundary tolerance by minor additions of Hf and B in a second generation single crystal superalloy. *Acta Mater.* **176**, 109–122 (2019).
34. L. J. Santodonato, P. K. Liaw, R. R. Unocic, H. Bei, J. R. Morris, Predictive multiphase evolution in Al-containing high-entropy alloys. *Nat. Commun.* **9**, 4520 (2018).
35. A. Pathak, A first principles calculation of site occupancy of the B2 phase in Ti_2AlX (X=V, Cr, Fe, Mo, Ta, Nb, Zr, Hf and Re) intermetallics. *Chin. J. Phys.* **60**, 339–344 (2019).
36. F. Körmann, T. Kostiuchenko, A. Shapeev, J. Neugebauer, B2 ordering in body-centered-cubic AlNbTiV refractory high-entropy alloys. *Phys. Rev. Mater.* **5**, 053803 (2021).

37. B. Feng, M. Widom, Elastic stability and lattice distortion of refractory high entropy alloys. *Mater. Chem. Phys.* **210**, 309–314 (2018).
38. O. N. Senkov, J.-P. Couzinie, S. I. Rao, V. Soni, R. Banerjee, Temperature dependent deformation behavior and strengthening mechanisms in a low density refractory high entropy alloy $Al_{10}Nb_{15}Ta_5Ti_{30}Zr_{40}$. *Materialia* **9**, 100627 (2020).
39. R. R. Eleti, N. Stepanov, N. Yurchenko, D. Klimenko, S. Zherebtsov, Plastic deformation of solid-solution strengthened Hf-Nb-Ta-Ti-Zr body-centered cubic medium/high-entropy alloys. *Scr. Mater.* **200**, 113927 (2021).
40. C. Rentenberger, H. P. Karnthaler, On the evolution of a deformation induced nanostructure in a Ni_3Al alloy. *Acta Mater.* **53**, 3031–3040 (2005).
41. S. Sheikh, S. Shafeie, Q. Hu, J. Ahlström, C. Persson, J. Veselý, J. Zýka, U. Klement, S. Guo, Alloy design for intrinsically ductile refractory high-entropy alloys. *J. Appl. Phys.* **120**, 164902 (2016).
42. C. Wen, C. Wang, Y. Zhang, S. Antonov, D. Xue, T. Lookman, Y. Su, Modeling solid solution strengthening in high entropy alloys using machine learning. *Acta Mater.* **212**, 116917 (2021).
43. G. Vazquez, P. Singh, D. Sauceda, R. Couperthwaite, N. Britt, K. Youssef, D. D. Johnson, R. Arróyave, Efficient machine-learning model for fast assessment of elastic properties of high-entropy alloys. *Acta Mater.* **232**, 117924 (2022).
44. M.-H. Tsai, K.-Y. Tsai, C.-W. Tsai, C. Lee, C.-C. Juan, J.-W. Yeh, Criterion for sigma phase formation in Cr- and V-containing high-entropy alloys. *Mater. Res. Lett.* **1**, 207–212 (2013).
45. X. J. Gu, S. J. Poon, G. J. Shiflet, M. Widom, Ductility improvement of amorphous steels: Roles of shear modulus and electronic structure. *Acta Mater.* **56**, 88–94 (2008).
46. X. J. Gu, S. J. Poon, G. J. Shiflet, M. Widom, Mechanical properties, glass transition temperature, and bond enthalpy trends of high metalloid Fe-based bulk metallic glasses. *Appl. Phys. Lett.* **92**, 161910 (2008).
47. B. Feng, M. Widom, Band structure theory of the bcc to hcp Burgers distortion. *Phys. Rev. B* **98**, 174108 (2018).
48. V. Raghuraman, M. Widom, M. C. Gao, Nonlinear deformation and elasticity of BCC refractory metals and alloys. *Phys Rev Mater* **6**, 053601 (2022).
49. N. F. Mott, H. Jones, *The Theory of the Properties of Metals and Alloys* (Dover Publications, 1958).
50. R. Dronskowski, P. E. Blöchl, Crystal orbital Hamilton populations (COHP). Energy-resolved visualization of chemical bonding in solids based on density-functional calculations. *J. Phys. Chem.* **97**, 8617–8624 (1993).
51. M. Mihalkovič, M. Widom, First-principles calculations of cohesive energies in the Al-Co binary alloy system. *Phys. Rev. B* **75**, 014207 (2007).
52. U. Bhandari, M. R. Rafi, C. Zhang, S. Yang, Yield strength prediction of high-entropy alloys using machine learning. *Mater Today Commun* **26**, 101871 (2021).
53. P. Hohenberg, W. Kohn, Inhomogeneous electron gas. *Phys. Rev.* **136**, B864–B871 (1964).
54. W. Kohn, L. J. Sham, Self-consistent equations including exchange and correlation effects. *Phys. Rev.* **140**, A1133–A1138 (1965).
55. G. Kresse, J. Furthmüller, Efficient iterative schemes for ab initio total-energy calculations using a plane-wave basis set. *Phys. Rev. B* **54**, 11169–11186 (1996).
56. G. Kresse, D. Joubert, From ultrasoft pseudopotentials to the projector augmented-wave method. *Phys. Rev. B* **59**, 1758–1775 (1999).
57. J. P. Perdew, K. Burke, M. Ernzerhof, Generalized gradient approximation made simple. *Phys. Rev. Lett.* **77**, 3865–3868 (1996).
58. S. Maintz, V. L. Deringer, A. L. Tchougréeff, R. Dronskowski, LOBSTER: A tool to extract chemical bonding from plane-wave based DFT. *J. Comput. Chem.* **37**, 1030–1035 (2016).
59. M. C. Troparevsky, J. R. Morris, P. R. C. Kent, A. R. Lupini, G. M. Stocks, Criteria for predicting the formation of single-phase high-entropy alloys. *Phys. Rev. X* **5**, 011041 (2015).
60. K. Momma, F. Izumi, *VESTA 3* for three-dimensional visualization of crystal, volumetric and morphology data. *J. Appl. Cryst.* **44**, 1272–1276 (2011).
61. A. Guinier, *X-Ray Diffraction: In Crystals, Imperfect Crystals, and Amorphous Bodies* (Courier Corporation, 1963).
62. R. Tran, Z. Xu, B. Radhakrishnan, D. Winston, W. Sun, K. A. Persson, S. P. Ong, Surface energies of elemental crystals. *Sci. Data* **3**, 160080 (2016).
63. X. Z. Wu, R. Wang, S. F. Wang, Q. Y. Wei, Ab initio calculations of generalized-stacking-fault energy surfaces and surface energies for FCC metals. *Appl. Surf. Sci.* **256**, 6345–6349 (2010).
64. X. Wu, R. Wang, S. Wang, Generalized-stacking-fault energy and surface properties for HCP metals: A first-principles study. *Appl. Surf. Sci.* **256**, 3409–3412 (2010).
65. T. L. Achmad, W. Fu, H. Chen, C. Zhang, Z. G. Yang, First-principles calculations of generalized-stacking-fault-energy of Co-based alloys. *Comput. Mater. Sci.* **121**, 86–96 (2016).
66. B. Bienvenu, C. C. Fu, E. Clouet, Impact of magnetism on screw dislocations in body-centered cubic chromium. *Acta Mater.* **200**, 570–580 (2020).
67. P. Tu, Y. Zheng, C. Zhuang, X. Zeng, H. Zhu, A high-throughput computation framework for generalized stacking fault energies of pure metals. *Comput. Mater. Sci.* **159**, 357–364 (2019).
68. X.-T. Chen, L. Shao, N. Ding, J.-M. Duan, B.-Y. Tang, Stacking fault energy of basal plane for hexagonal closed-packed medium entropy alloy ZrHfTi: Ab initio prediction. *Appl. Phys. A* **127**, 670 (2021).
69. X. Wang, S. Xu, W. R. Jian, X. G. Li, Y. Su, I. J. Beyerlein, Generalized stacking fault energies and Peierls stresses in refractory body-centered cubic metals from machine learning-based interatomic potentials. *Comput. Mater. Sci.* **192**, 110364 (2021).
70. X. Zhang, J. Tang, L. Deng, G. Zhong, X. Liu, Y. Li, H. Deng, W. Hu, The effects of interstitial impurities on the mechanical properties of vanadium alloys: A first-principles study. *J. Alloys Compd.* **701**, 975–980 (2017).
71. R. Hill, The elastic behaviour of a crystalline aggregate. *Proc. Phys. Soc. A* **65**, 349 (1952).
72. A. Reuss, Berechnung der Fließgrenze von Mischkristallen auf Grund der Plastizitätsbedingung für Einkristalle. *Z. Angew. Math. Mech.* **9**, 49–58 (1929).
73. A. Takeuchi, A. Inoue, Classification of bulk metallic glasses by atomic size difference, heat of mixing and period of constituent elements and its application to characterization of the main alloying element. *Mater. Trans.* **46**, 2817–2829 (2005).
74. I. Toda-Caraballo, A general formulation for solid solution hardening effect in multicomponent alloys. *Scr. Mater.* **127**, 113–117 (2017).
75. C. Varvenne, A. Luque, W. A. Curtin, Theory of strengthening in fcc high entropy alloys. *Acta Mater.* **118**, 164–176 (2016).
76. Y. F. Ye, C. T. Liu, Y. Yang, A geometric model for intrinsic residual strain and phase stability in high entropy alloys. *Acta Mater.* **94**, 152–161 (2015).

Acknowledgments: M.W. acknowledges a discussion with Amit Samanta on the link between the Fermi level density of states and ductility. **Funding:** This work was supported by the Department of Energy under grant no. DE-SC0014506 (M.W.), the Office of Naval Research under grant no. N00014-23-1-2441 (J.Q., D.I.H., and J.P.), the National Science Foundation (DMR—1611180, 1809640, and 2226508) (X.F. and P.K.L.), the US Army Research Office (FA9550-23-1-0503, W911NF-13-1-0438, and W911NF-19-2-0049) (X.F. and P.K.L.), the Department of Energy (DOE DE-EE0011185) (P.K.L.), and the State of Tennessee and Tennessee Higher Education Commission (THEC) through their support of the Center for Materials Processing (CMP) at the University of Tennessee (X.F.). The present research used the resources of the National Energy Research Scientific Computing Center (NERSC), a US Department of Energy Office of Science User Facility operated under contract number DE-AC02-05CH11231, using the NERSC award, BES-ERCAP24744. (M.W.). **Author contributions:** Conceptualization: J.Q., M.W., J.P., and P.K.L. Methodology: J.Q., J.P., D.I.H., M.W., and P.K.L. Investigation: J.Q., X.F., D.I.H., and M.W. Visualization: J.Q. and M.W. Supervision: J.P., P.K.L., and M.W. Writing—original draft: J.Q., X.F., and M.W. Writing—review and editing: J.Q., J.P., and P.K.L. **Competing interests:** The authors declare that they have no competing interests. **Data and materials availability:** All data needed to evaluate the conclusions in the paper are present in the paper and/or the Supplementary Materials.

Submitted 22 April 2024
Accepted 30 October 2024
Published 4 December 2024
10.1126/sciadv.adq0083